Chemical Science

ROYAL SOCIETY OF CHEMISTRY

EDGE ARTICLE

View Article Online
View Journal | View Issue

Check for updates

Cite this: *Chem. Sci.*, 2022, **13**, 4555

All publication charges for this article have been paid for by the Royal Society of Chemistry

Received 3rd November 2021
Accepted 16th March 2022

DOI: 10.1039/d1sc06098h

rsc.li/chemical-science

Growth kinetics determine the polydispersity and size of PbS and PbSe nanocrystals†

Michael P. Campos,‡[a] Jonathan De Roo, ‡[ab] Matthew W. Greenberg,‡[a] Brandon M. McMurtry, ‡[a] Mark P. Hendricks,[ai] Ellie Bennett, [a] Natalie Saenz,[a] Matthew Y. Sfeir, [cde] Benjamin Abécassis, [fg] Sanjit K. Ghose[h] and Jonathan S. Owen *[a]

A library of thio- and selenourea derivatives is used to adjust the kinetics of PbE (E = S, Se) nanocrystal formation across a 1000-fold range ($k_r = 10^{-1}$ to 10^{-4} s^{-1}), at several temperatures (80–120 °C), under a standard set of conditions (Pb : E = 1.2 : 1, [Pb(oleate)$_2$] = 10.8 mM, [chalcogenourea] = 9.0 mM). An induction delay (t_{ind}) is observed prior to the onset of nanocrystal absorption during which PbE solute is observed using *in situ* X-ray total scattering. Density functional theory models fit to the X-ray pair distribution function (PDF) support a $Pb_2(\mu_2\text{-}S)_2(Pb(O_2CR)_2)_2$ structure. Absorption spectra of aliquots reveal a continuous increase in the number of nanocrystals over more than half of the total reaction time at low temperatures. A strong correlation between the width of the nucleation phase and reaction temperature is observed that does not correlate with the polydispersity. These findings are antithetical to the critical concentration dependence of nucleation that underpins the La Mer hypothesis and demonstrates that the duration of the nucleation period has a minor influence on the size distribution. The results can be explained by growth kinetics that are size dependent, more rapid at high temperature, and self limiting at low temperatures.

Introduction

Across a wide range of materials, colloidal nanocrystals can be synthesized with surprising monodispersity.[1,2] In many of these syntheses, the kinetics of nanocrystal formation are limited by the irreversible conversion of synthesis precursors to units of the growing crystal. Under such conditions, the temporal evolution of the precipitation can be controlled by the precursor reactivity. In the case of noble metal nanocrystals, for example, the conversion of metal salt precursors is thought to be autocatalytic and occurs at the nanoparticle surface.[3–5] On the other hand, metal chalcogenide,[6–12] and in some cases, gold[13,14] nanocrystals are believed to form by assembly of soluble molecular intermediates produced by the conversion of precursors in homogeneous solution. While nucleation and growth are inherently autocatalytic, as described by Finke and Watzky,[15] if the formation of solutes by the precursor reaction is substantially slower than crystal growth, the precipitation kinetics will be governed by the precursor conversion reaction, and the size of the final nanocrystal will be controlled by the precursor reactivity.[16]

A variety of nanocrystal precursors have been designed to adjust the rate at which InP,[17–21] CdTe,[22] CdSe,[12,23] CdS,[2,24,25] PbSe,[26–29] PbS,[30] $Cu_{2-x}S$,[30] Fe_xS_y,[31] $CuInSe_2$,[32] $CuInS_2$,[33] and ZnS[34] solute is produced. Among these, chalcogenourea derivatives finely adjust the formation of metal chalcogenides over more than a million-fold range of reactivity (Scheme 1).[2] The wide range of fine control over the solute supply provides several advantages that simplify synthesis. For example, the precursor reactivity can be appropriately chosen to match the desired crystallization temperature; the nucleation onset can be delayed until the synthesis mixture has achieved a homogeneous composition following the injection, improving the reproducibility and facilitating mechanistic studies;[35] the final nanocrystal size can be controlled without modifying other aspects of the synthesis such as the surfactant composition, the precursor

---

[a] Department of Chemistry, Columbia University, New York, New York 10027, USA. E-mail: jso2115@columbia.edu

[b] Department of Chemistry, University of Basel, Basel 4058, Switzerland

[c] Center for Functional Nanomaterials, Brookhaven National Laboratory, Upton, New York 11973, USA

[d] Photonics Initiative, Advanced Science Research Center, City University of New York, New York, New York 10031, USA

[e] Department of Physics, Graduate Center, City University of New York, New York, New York 10016, USA

[f] ENSL, CNRS, Laboratoire de Chimie UMR 5182, 46 allée d'Italie, 69364 Lyon, France

[g] Université Paris-Saclay, CNRS, Laboratoire de Physique des Solides, 91405 Orsay, France

[h] National Synchrotron Light Source II, Brookhaven National Laboratory, Brookhaven, New York, USA

[i] Department of Chemistry, Whitman College, Walla Walla, Washington 99362, USA

† Electronic supplementary information (ESI) available. See DOI: 10.1039/d1sc06098h

‡ M. P. C., J. D. R., M. W. G., and B. M. M. contributed equally to this work.

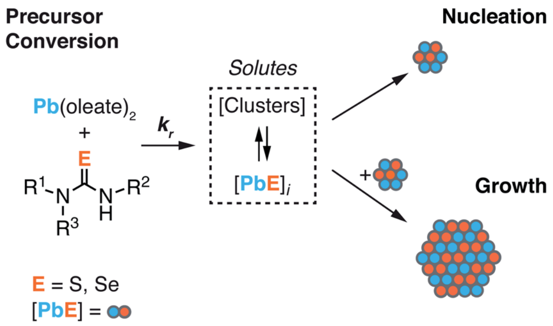

Scheme 1 Lead oleate and chalcogenourea precursors undergo irreversible conversion to solutes. Solutes undergo consumption by competitive nucleation and growth pathways. The size of nuclei is unknown and is not indicated by the size shown in Scheme 1.

concentrations, or quenching the precursor reaction to limit the yield.[8,12] These advantages have made it possible to demonstrate a well behaved relationship between the solute supply rate and the final nanocrystal concentration in several materials.[2,8,12,17,30,34,36]

Nucleation mass balance models developed by Sugimoto describe the connection between solute supply kinetics and the extent of nucleation.[9,37,38] These models illustrate how the rate of solute supply during nucleation and the rate of solute consumption by growth dictate the number of crystals that are nucleated ($[\mathrm{NC}]_{\mathrm{final}}$). A competition between the growth and the nucleation manifolds for the available solutes governs the extent of nucleation and the final size. In other words, slow growth kinetics can lead to greater numbers of smaller nanocrystals, provided that the role of aggregation and ripening are also considered.

In the present study we investigate the influence of temperature on the final nanocrystal size using nucleation mass balance models as a guide. We leverage the range of reactivity provided by *N*,*N*′-di and *N*,*N*,*N*′-trisubstituted chalcogenoureas to independently adjust the solute supply kinetics at several temperatures and infer the temperature dependence of the growth rate from the final nanocrystal size. The absence of nanocrystal ripening and the very narrow size distributions that are characteristic of our model system allow precise determination of the number of nanocrystals formed during nucleation.[26,30,39] In addition, we identify conditions where the kinetics of nucleation can be directly observed, as well as conditions where the solutes that accumulate prior to nucleation can be probed with X-ray scattering.

Experimental

General methods

The model nanocrystal synthesis using lead oleate, thio-, and selenoureas is described elsewhere.[30,36]

Synthesis of PbS and PbSe nanocrystals

In situ kinetics are obtained as previously described.[30] Briefly, in a nitrogen-filled glovebox, three vessels are prepared: (A) lead oleate (166.3 mg, 0.216 mmol, 1.2 equiv.) and hexadecane (19.0 mL) in a 25 mL three-neck round-bottom flask, sealed with three rubber septa. (B) The desired thio- or selenourea (0.216 mmol, 1.2 equiv.) and diphenyl ether (1.288 g, 1.2 mL) are added to a 4 mL scintillation vial, sealed with a rubber septum. (C) Tetrachloroethylene (3.895 g, 2.4 mL) is added to a 1 cm × 1 cm quartz cuvette, sealed with a septum cap. The vessels A and B are then attached to a Schlenk line *via* argon inlet needles and the *in situ* optical dip probe is installed under positive argon flow. Both vessels are equilibrated in oil baths set to the desired temperature (>15 minutes). After baseline correction, the recording of the absorbance at 400 nm is started, collecting one data point every 600 ms. The thio- or selenourea solution (1 mL, 0.180 mmol, 1.0 equiv) is injected into the lead oleate solution to initiate the reaction. This results in 20 mL of total solution with a lead oleate concentration of 10.8 mM and a thio- or selenourea concentration of 9.0 mM. The reaction is run for 7–9 half lives ($t_{1/2}$), at which time the absorbance reaches a plateau. At this time, a 100 μL aliquot is removed and added to the cuvette containing 2.4 mL of tetrachloroethylene to measure the full UV-vis-NIR absorption spectrum.

Determination of [PbS] and k_r from *in situ* absorbance

The kinetics of PbS and PbSe nanocrystal formation are measured from the absorbance at $\lambda = 400$ nm according to our previous report (Fig. 1).[30] At this wavelength the absorbance is independent of NC size and proportional to the number of PbS or PbSe units in nanocrystals (see Discussion Section).[40] However, the correlation between the molar concentration of crystalline material and the absorptivity at 400 nm may depend

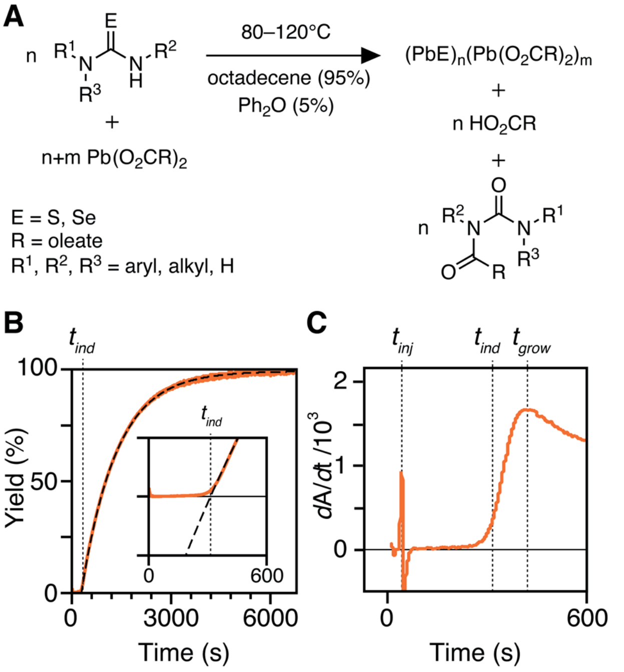

Fig. 1 (A) Precursor conversion reaction stoichiometry and conditions in this study. (B) *In situ* absorption traces with single exponential fit (dashed line) with inset showing the absorption onset. (C) First derivative of trace shown in B with the associated t_{inj}, t_{ind}, and t_{grow} labeled with dotted lines.

on the size below diameters of 2 nm (~80 PbE units), which prevents a detailed interpretation of the absorption onset. Regardless, the majority of syntheses studied here produce nanocrystals of much larger size and the absorbance following the onset is a reliable measure of the PbS or PbSe units in crystalline material.[41–43]

An example dip probe trace is displayed in Fig. 1B and C. Two maxima can be observed in the derivative, the first corresponding to the injection time, t_{inj}, and the second corresponding to the time after which the absorbance trace displays single-exponential behavior, t_{grow}. The data following t_{grow} were fit to a single exponential function:

$$A = A_{\text{final}}(1 - e^{-k_r(t - t_{\text{ind}})}) \tag{1}$$

where A_{final} is the maximum absorption reached, k_r is a rate constant, and t_{ind} is the time where the exponential fit intersects the x-axis ($t_{\text{inj}} = 0$). Although many traces are well described by a single exponential, some have more complex functional forms and the quality of a single exponential fit at early times does not properly capture the absorption onset. To ensure the t_{ind} is precisely determined, A_{final} is first determined from the fit of the full data set, and then used to constrain a fit of the points between $A(t_{\text{grow}})$ and $3A(t_{\text{grow}})$. This fitting method preferentially weights the early time data and describes the full data set well (see ESI†). Weighting the early time data reliably captures the absorption onset. The early time fits modify the k_r and t_{grow} obtained from fits of the full dataset by 10% or less, which we, therefore, use as an estimate of the uncertainty in these quantities.

We postulate that the precursor conversion reaction starts at the moment of injection. Using eqn (1), we calculate the concentration of PbE formed during the induction delay, by assuming that k_r is equal to the precursor conversion rate constant. The fraction of precursor conversion during the induction delay (f_{ind}) is calculated according to eqn (2):

$$f_{\text{ind}} = \frac{-A_0}{-\mathrm{A}_0 + \mathrm{A}_{\text{final}}} \tag{2}$$

and the lead chalcogenide concentration at the end of the induction delay can be estimated according to eqn (3) using the $[\text{PbE}]_{\text{final}}$, calculated from the final UV-vis-NIR spectrum.

$$[\text{PbE}]_{\text{ind}} = [\text{PbE}]_{\text{final}} \times f_{\text{ind}} \tag{3}$$

The $[\text{PbE}]_{\text{ind}}$ measured in this way is an underestimate of the solute concentration at t_{ind} because the k_r under estimates the precursor conversion reactivity. However, the difference is small, as demonstrated in a study to be published elsewhere.[44]

Measurement of nucleation kinetics, nucleation fraction, and yield using UV-Vis-NIR absorption of aliquots

Quantitative aliquots (0.2 mL) are taken to monitor the nucleation process. Aliquots are injected into a pre-weighed vial in air and immediately cooled to −78 °C to prevent further precursor conversion. Immediate freezing of aliquots causes a feature to appear in the absorption spectrum (λ ~475 nm) that is assigned to PbS solutes (see below).[45] Each aliquot is weighed and diluted with a known amount of tetrachloroethylene (3 mL) prior to recording a UV-Vis-NIR absorption spectrum. A background spectrum was recorded from a known mass of hexadecane and diphenyl ether diluted in tetrachloroethane. The background spectrum was subtracted from the UV-Vis-NIR spectra of aliquots by accounting for the concentration of the hexadecane and diphenyl ether in the aliquot solution. In this way the vibrational overtones of the solvent can be reduced.[46]

The intensity and wavelength of the lowest energy excitonic transition provides a direct measure of the nanocrystal concentration that is unaffected by the absorbance of solutes. Using a size-dependent extinction coefficient the absorbance intensity at the lowest energy excitonic feature is converted to the [NC] at each time point according to a previously described method.[47] By using the lowest energy excitonic absorption intensity rather than the absorbance at $\lambda = 400$ nm we avoid measuring the absorbance of solutes, which can be misinterpreted as nanocrystal absorbance.[45,48,49] On the other hand, upon complete precursor conversion the [NC] reaches a plateau and the solute concentration is assumed to be insignificant. At this point, the $[\text{NC}]_{\text{final}}$ is determined using the absorbance at $\lambda = 400$ nm.[40,48] (see ESI†).

Measurements of [NC] taken from the lowest energy excitonic absorbance intensity do not consider the influence of the polydispersity or surface chemistry on the breadth and intensity of the excitonic transition. Mechanisms that induce broadening of this transition (*e.g.* Ostwald Ripening) will systematically influence the [NC]. However, the broadening caused by the polydispersity of our samples is less than 25% of the total width at reaction temperatures from 90–120 °C (Fig. S28 and S29†), which helps to mitigate this effect. Nonetheless, at high temperatures, a decrease in the observed [NC] can be observed in one case (Fig. S25†).

By measuring the nanocrystal concentration during the synthesis, we can directly determine the rate at which crystallites are produced, a process we define as nucleation. Although our measurement does not capture crystallites much smaller than the ensemble average, this is a minor consideration given the narrow polydispersities that are observed at all time points. While, in principle, ripening and agglomeration can influence the nanocrystal concentration and obscure the nucleation kinetics, these pathways are insignificant at the end of the reaction, as was described in our recent reports.[26,30] Moreover, it is consistent with the observation that the concentration of nanocrystals becomes stable after an initial period (Fig. S25†).

Plots of [NC] *versus* time were fitted to a single exponential to extract an observed nucleation rate constant $k_{[\text{NC}]}$ where [NC] is the concentration of nanocrystals at time t, and $[\text{NC}]_{\text{final}}$ is the final concentration of nanocrystals (eqn (4)). Example fittings are provided in the ESI.† While the true functional form of the nucleation process is unlikely to be first order, the $k_{[\text{NC}]}$ provides a convenient method for comparing the relative rates of nucleation and the precursor reaction as the temperature is varied.

$$[\text{NC}] = [\text{NC}]_{\text{final}}(1 - e^{-k_{[\text{NC}]}(t - t_{\text{ind}})}) \tag{4}$$

The nucleation kinetics were compared to the kinetics of the yield development in aliquots by measuring the $[PbS]_i$ using a size independent extinction coefficient ($\lambda = 400$ nm). The yield at each time point can also be measured directly from the intensity of the excitonic transition, however, we chose to use the absorbance at $\lambda = 400$ nm to capture the absorbance of small clusters, thus providing a better approximation of the precursor conversion kinetics. To account for variations in the amount of aliquoted material in the cuvette, the measured $[PbS]_i$ in the cuvette was corrected using the mass of reaction solution and the tetrachloroethylene solvent. The kinetics of PbS formation were determined by fitting the temporal evolution of $[PbS]_i$ to the following equation where $[PbS]_{final}$ is the final concentration of $[PbS]_i$ (eqn (5)).

$$[PbS]_i = [PbS]_{final}(1 - e^{-k_r(t - t_{ind})}) \tag{5}$$

The extracted rate constants ($k_{[NC]}$ and k_r) are used to calculate half-lives of the nucleation and precursor conversion reactions ($t_{1/2,[NC]} = \ln(2)/k_{[NC]}$ and $t_{1/2,rxn} = \ln(2)/k_r$). The ratio of $t_{1/2,[NC]}$ and $t_{1/2,rxn}$, a so called nucleation fraction, allows the relative duration of the nucleation and growth processes to be compared (see ESI† for details).[17]

In situ total scattering measurements/pair distribution function analysis

Experiments are carried out using beamline 28-ID-2 at the National Synchrotron Light Source II (NSLS-II) at Brookhaven National Laboratory. X-ray scattering data are collected at room temperature, in rapid acquisition mode, using a 2D PerkinElmer amorphous silicon detector (2048 × 2048 pixels and 200 × 200 μm pixel size) with a sample to detector distance of 202.444 mm. The incident wavelength of the X-rays is $\lambda = 0.1877$ Å (66.05 keV). Calibration of the experimental setup is performed using a nickel standard sample.

In situ X-ray scattering experiments are performed using a custom designed reactor consisting of a remotely controlled injector, a three neck flask equipped with a temperature probe, a magnetic stirrer, an argon inlet, and submerged in an oil bath. A Hei-FLOW Precision 01 peristaltic pump, and Viton tubing (Cole-Parmer, 1/16″ID × 1/8″OD) connects a stainless steel syringe needle to a custom Kapton X-ray flow cell. Precursor injection and triggering of the peristaltic pump are both controlled remotely, allowing diffraction patterns to be collected with the shortest time delay possible following mixing of precursors.

The reaction is initiated by a remotely triggered injection of 7 mL of a 190 mM diglyme solution of an *N*,*N*′-disubstituted thiourea or *N*,*N*–*N*′-trisubstituted selenourea (1.33 mmol) into 143 mL of a 11.3 mM solution of lead oleate (1.62 mmol) at 80 °C or 110 °C under argon with stirring. The thiourea and selenourea used for the PbS and PbSe reactions at 80 °C are *N*-3,5-bis-trifluoromethylphenyl-*N*′-dodecylthiourea and *N*-cyclohexyl-2-methylpyrrolidine-1-carboselenoamide, respectively. At 110, °C *N*-*p*-methoxyphenyl-*N*′-dodecylthiourea and *N*-butylpyrrolidine-1-carboselenoamide were chosen for their relatively slow reactivity ($k_S = 1.69 \times 10^{-3}$ s^{-1}, $k_{Se} = 2.21 \times 10^{-3}$ s^{-1}) and similar precursor conversion kinetics. The resulting solution is 10.8 mM (1.2 equiv.) in lead and 8.90 mM (1.0 equiv.) in chalcogen immediately following injection. Following the precursor injection, the peristaltic pump is run at maximum speed for ten seconds to ensure the reaction mixture has reached the X-ray beam and passed through the remainder of the Viton tubing into a waste container that is also under Ar. Following this 10 second period, the flow rate is immediately and automatically set to a slower setting which was experimentally measured to be 4.0 mL min^{-1} under reaction conditions. After reducing the pumping speed, the acquisition of 30 second X-ray scattering patterns is initiated. Based on the pump rates and reaction volume contained in the Viton tubing, the "in flask" reaction time for each spectrum is estimated as described in the ESI.† An X-ray scattering pattern of the lead(II) oleate precursor solution was acquired over 15 minutes at the reaction temperature by circulating the precursor through the flow cell.

Raw 2D data are corrected for geometrical effects and polarization, then azimuthally integrated to produce 1D scattering intensities *versus* the magnitude of the momentum transfer Q (where $Q = 4\pi \sin \theta/\lambda$ for elastic scattering) using the program Fit2D.[50] The program xPDFsuite with PDFgetX3 is used to perform the background subtraction, further corrections, and normalization to obtain the reduced total scattering structure function $F(Q)$, and Fourier transformation to obtain the pair distribution function (PDF), G.[51,52] The Q_{min} is determined by the beamstop.

PDFs are processed with a low Q_{max} ($Q_{max} = 10.0$ Å^{-1}) to reduce statistical noise in order to evaluate low amplitude signals during early reaction time points. Once nanocrystals have formed following nucleation this can be extended out further to 15.0–20.0 Å^{-1} with only minor effects on the data quality in $G(r)$ (Fig. S12†). Virtual crystal modeling of PbS and PbSe nanoparticle growth is performed using PDFGui, and is described in further detail in the ESI†.[53]

Results

PbS and PbSe nanocrystals were synthesized using thiourea and selenourea reagents with conversion reactivities between 10^{-1} to 10^{-4} s^{-1} at 80–140 °C. Under the conditions studied herein, the induction delay (t_{ind}) prior to the appearance of species that absorb $\lambda = 400$ nm photons ranges from less than a second to several minutes depending on the material and the precursor reactivity (Fig. 2). At 80 °C the t_{ind} prior to the appearance of PbSe absorption is an order of magnitude shorter than the appearance of PbS under nearly identical solute generating conditions ($k_r^{Se} = 1.6 \times 10^{-3}$ s^{-1} *vs.* $k_r^{S} = 1.7 \times 10^{-3}$ s^{-1}) (Fig. 2A). PbSe reactions display shorter t_{ind} than PbS reactions over a wide range of conversion reactivity (Fig. 2B). While t_{ind} of a few seconds is typical for PbSe, an induction delay exceeding a minute is not uncommon for PbS. In particular, syntheses of PbSe at high temperature (120 °C) have little delay prior to the absorption onset. At this temperature, the delay times are likely influenced by the kinetics of mixing and are insensitive to the precursor reactivity (Fig. S4†). The correlation between the t_{ind} and k_r over a wide range demonstrates systematic and

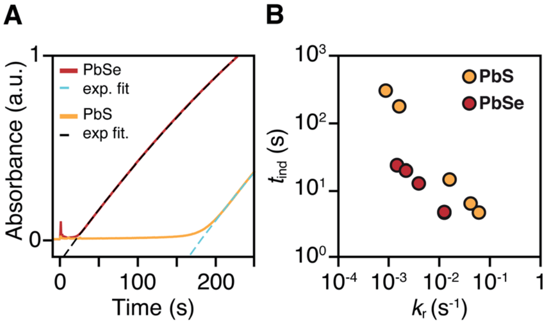

Fig. 2 (A) *In situ* absorption at $\lambda = 400$ nm during nucleation onset in the synthesis of PbS (yellow) and PbSe (red) from *N*-3,5-bis(trifluoromethyl)phenyl-*N*′-dodecylthiourea and *N*,*N*-dimethyl-*N*′-cyclohexylselenourea, which have similar conversion reactivity ($k_r(S) = 1.7 \times 10^{-3}$ s^{-1}, $k_r(Se) = 1.6 \times 10^{-3}$ s^{-1}). (B) Comparison of t_{ind} and k_r for several thio-and selenoureas at 80 °C showing that the induction delay is consistently longer when synthesizing PbS.

reproducible reaction conditions over a wide range of conditions in both material systems.

The concentration of solute at t_{ind} was estimated across two orders of magnitude in the reaction rate and a 30 or 40 °C range of temperature (Fig. 3). PbS reactions reach an order of magnitude higher solute concentrations prior to the development of absorbance at $\lambda = 400$ nm ($[PbS]_{ind} = 1.0$–2.9 mM, $[PbSe]_{ind} = 0.15$–0.58 mM). These are relatively high concentrations in the case of PbS, and clearly indicate that solutes do not absorb visible light until a larger size is achieved.

As much as 11–32% of the total added sulfur and 1–7% of the total added selenium accumulates as solutes prior to contributing to the absorbance at $\lambda = 400$ nm. Moreover, these concentrations are 10–100x greater than the concentration of nanocrystals formed by nucleation (see below). Thus, the solutes produced during the induction time undergo assembly into nuclei and nanocrystals, consistent with a homogeneous nucleation and growth mechanism.

The $[PbE]_{ind}$ depends on both the temperature and the k_r. Interestingly, the $[PbE]_{ind}$ observed in PbSe syntheses more than doubles over an order of magnitude increase in k_r. The increase suggests that the kinetics of $[PbSe]_i$ generation are similar to the kinetics of the precipitation. The growth of PbS, on the other hand, displays a relatively consistent $[PbE]_{ind}$. These results suggest that larger nanostructures form at a lower $[PbE]_{ind}$ in the case of PbSe. However, differences in the absorptivity of small PbS *vs.* PbSe clusters could also explain these results.

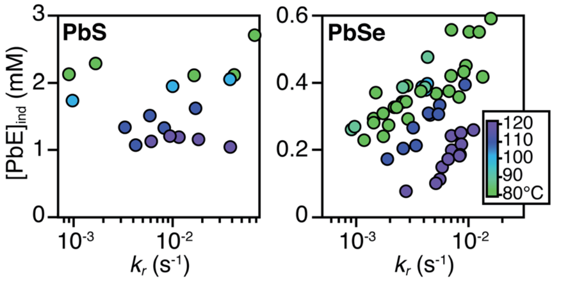

Fig. 3 Plots of $[PbE]_{ind}$ solute at (t_{ind}) *versus* k_r for (A) PbS and (B) PbSe.

X-ray pair distribution function analysis of early reaction times

To determine the structure of solutes and crystals present during the induction delay, nucleation, and growth stages, *in situ* synchrotron X-ray total scattering and pair distribution function (PDF) analysis experiments were performed. X-ray PDF has previously been used to study the evolution of metal oxide solutes and nanocrystals (*e.g.*, WO_3, SnO_2) during hydrothermal synthesis,[54–56] and the structures formed during the early stages during metal organic framework synthesis.[57]

At the standard 9 mM concentration used in this study, 30 seconds of acquisition time was required to achieve sufficient signal to perform PDF analysis. This time resolution allowed PDFs to be obtained prior to t_{ind} when a relatively slowly reacting thiourea (*N*-3,5-bis-trifluoromethylphenyl-*N*′-dodecylthiourea, $k_r = 1.7 \times 10^{-3}$ s^{-1}, $t_{ind} = 182$ s) is used (Fig. 4A). These measurements revealed correlations with $r < 1$ nm that evolve to structures with longer range correlations during the absorption onset. Similar measurements on a PbSe nanocrystal synthesis with comparable kinetics (*N*-cyclohexyl-2-methylpyrrolidine-1-carboselenoamide, $k_r = 2.2 \times 10^{-3}$ s^{-1}, $t_{ind} = \sim 20$ s) showed a much more rapid development of long

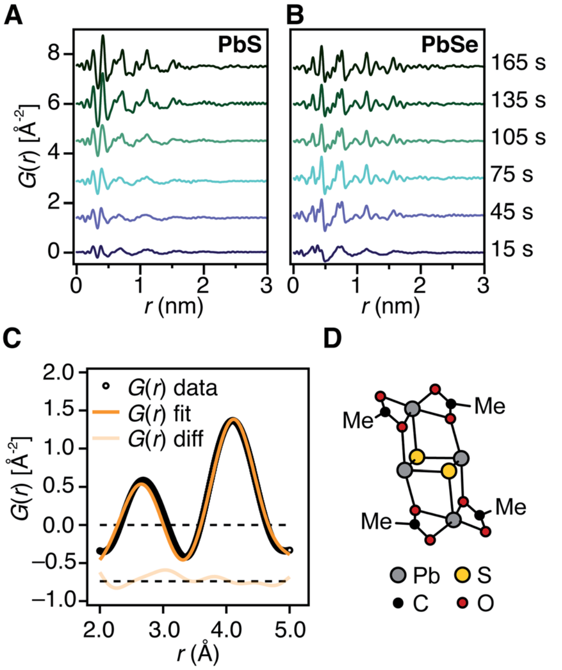

Fig. 4 Early time *in situ* X-ray PDF measurements of PbS and PbSe nanocrystal reactions at 80 °C using (A) *N*-3,5-bis-trifluoromethylphenyl-*N*′-dodecylthiourea and (B) *N*-cyclohexyl-2-methylpyrrolidine-1-carboselenoamide, respectively. These reactions proceed with comparable precursor conversion kinetics. (C) Fit of low *r* correlations ($r = 0.2$–0.5 nm) from an early-time PDF pattern collected prior to the absorption onset at 110 °C using the candidate structure shown in (D). The displayed fit has an $R_w = 0.1045$. (D) DFT structure of $(Pb_2(\mu_2\text{-}S)_2(Pb(acetate)_2)_2)$.

range atomic pair correlations (Fig. 4B). The shorter induction periods prior to optical absorption from PbSe correlates with more rapid appearance of long-range Pb–Se atomic order. This can also clearly be seen in reciprocal space with the appearance of prominent [111], [200], [220], [311], [222] reflections of a rock salt lattice appearing more rapidly in the case of PbSe *versus* PbS (Fig. S10 and S11†). These observations support the conclusion that the onset of optical absorption at $\lambda = 400$ nm is characteristic of mature nanostructures with longer range atomic pair correlations. The colorless solutions prior to this time contain relatively high concentrations of molecular solutes formed by precursor conversion.

The PDF patterns were fit using a periodic PbS or PbSe rock salt model and a spherical envelope dampening function, to estimate the crystallite size at each time point (Fig. 4C and S14–S15†).[58] A residual fit function (R_w) was calculated for each pattern, the magnitude of which is indicative of the fit quality. At early times, the R_w is greatest and slowly decreases to its terminal value several minutes following nucleation (Fig. S13†). Thus the rock salt model does not adequately capture the structure of solutes at early times (Fig. S16†).

PDF patterns prior to t_{ind}, show nearest (*e.g.* Pb–S), second nearest (*e.g.* Pb–Pb and S–S), and third nearest neighbor correlations that are distinct from lead oleate in solution or the solid state and consistent with the formation of molecular PbS solutes (Fig. S17–S21†). Following t_{ind}, the PDF data is accurately captured by the spherical nanocrystal model. Several hypothetical discrete PbS solute structures were computed using density functional theory, and their PDFs compared to the experimental data. Among these, a Pb_2S_2 diamond bound by lead carboxylate (*e.g.*, $Pb_2(\mu_2\text{-}S)_2(Pb(O_2CR)_2)_2$) accurately recovers the ratio of the first and second nearest neighbor correlations (Fig. 4C and D). Moreover the PDF pattern evolves with time, temperature, and concentration in a manner that is consistent with a variety of solute structures being present. Assigning the atomic structure of these early solute species and their individual concentrations requires more detailed analysis. However, the correlations present during the induction delay are inconsistent with ordered structures larger in size than $Pb_2(\mu_2\text{-}S)_2(Pb(O_2CR)_2)_2$. Thus, we conclude that the solutes accumulating prior to the induction delay are molecular and then slowly assemble into nanocrystals.

Size control

The influence of the precursor reactivity and temperature on the $[NC]_{\text{final}}$ is shown below in Fig. 5. Both low temperatures and more reactive thio- and selenoureas afford a higher $[NC]_{\text{final}}$ and a smaller final diameter.[30,36] The results are consistent with nucleation mass balance models described by Sugimoto and others,[9,37,38] where the growth kinetics increase with increasing temperature. Similarly, under otherwise identical conditions, PbSe nanocrystals reach larger sizes than PbS, which can be attributed to faster growth kinetics.

Interestingly, the final size of both PbSe and PbS nanocrystals becomes more sensitive to the precursor reactivity at high temperature, while at the lowest temperature the size remains within 3–4 nm over more than an order of magnitude spread in precursor reactivity. The small range of sizes produced at low temperatures suggests that growth is slow and nucleation continues over long periods. To probe this hypothesis, the nucleation kinetics were monitored with optical spectroscopy.

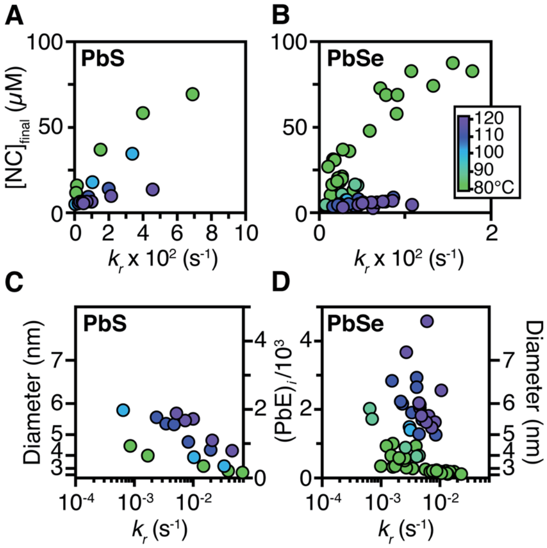

Fig. 5 The $[NC]_{\text{final}}$ from syntheses of (A) PbS and (B) PbSe were measured from the spectrum of an aliquot at the end of each reaction. The final average size and number of PbE units per nanocrystal for the (C) PbS and (D) PbSe reactions studied herein.

Nucleation time and polydispersity

To measure the nucleation kinetics, the optical spectrum of timed aliquots is analyzed to extract the [NC] throughout the synthesis. Fig. 6 illustrates a typical spectral evolution and plots the evolving [NC] and $[PbE]_i$. In addition to the steady red shift of the lowest energy excitonic feature, a second feature is visible at high energies ($\lambda_{\text{max}} = 475$–$510$ nm) that persists over the first half of the reaction (Fig. S5†).[45] Interestingly, this higher energy

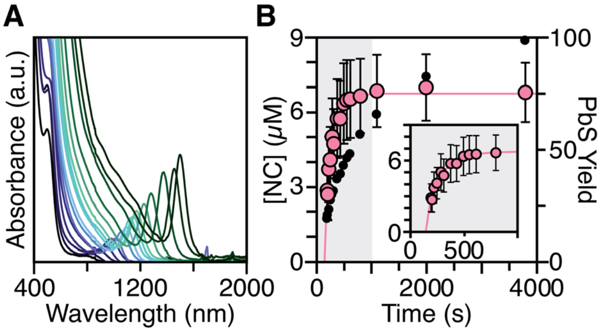

Fig. 6 (A) Evolution of the UV-Vis-NIR absorbance spectrum for a reaction of $Pb(oleate)_2$ with *N*-4-methoxyphenyl-*N*′-dodecylthiourea at 90 °C. (B) Temporal evolution of [NC] (pink) and PbS yield (black). The shaded portion of the plot is replotted in the inset and shows the extended nucleation period. See the ESI† for a discussion of the uncertainty shown.

feature is absent if aliquots are not immediately quenched in an acetone-dry ice bath. We hypothesize that molecular PbS solutes present at the reaction temperature assemble into clusters with an absorbance feature at 475 nm upon rapid cooling.

To avoid complications from the high energy feature, the temporal evolution of the [NC] extracted from the energy and intensity of the lowest energy excitonic feature was measured across a range of precursor reactivities and reaction temperatures. A slow steady increase in the number of nanocrystals is observed, especially at low temperatures (Fig. 6B and S25†). We have observed similarly prolonged nucleation under identical conditions using *in situ* X-ray scattering measurements that will be reported elsewhere.[44] The increasing nanocrystal concentrations observed here provide a direct measure of the nucleation kinetics because the final nanocrystals do not significantly ripen or agglomerate under these conditions.[26,30] Hence, the steadily increasing [NC] shows that crystal nucleation continues throughout a significant fraction of the total reaction time rather than occurring in a burst.

The length of the nucleation period is estimated by fitting the [NC] *versus* time using eqn (5). Half-lives of the nucleation and precursor conversion reactions ($t_{1/2,[\mathrm{NC}]} = \ln(2)/k_{[\mathrm{NC}]}$ and $t_{1/2,\mathrm{rxn}} = \ln(2)/k_\mathrm{r}$) are extracted and compared to understand the duration of the nucleation period (see ESI† for details).[17] Fig. 7A plots the nucleation fraction at several temperatures and demonstrates that the nucleation period occurs in a smaller fraction of the reaction time as the temperature is increased. At temperatures > 120 °C the nucleation occurs more rapidly than could be measured, while at the lowest temperatures, nucleation persists for > 50% of the synthesis. The long nucleation times starkly contrast with the so called "burst" of nucleation typically ascribed to monodisperse ensembles of nanocrystals.

The full width at half maximum (FWHM) of the lowest energy excitonic absorbance feature of the final PbS nanocrystals is shown in Fig. 7B. A hole burning transient absorption method previously employed to study PbSe nanocrystals was used to estimate the intrinsic FWHM of several sizes and is shown for comparison.[26] These measurements demonstrate that the spectral linewidth of the nanocrystals prepared here are dominated by the intrinsic breadth of a single size rather than the polydispersity. Moreover, the intrinsic linewidth narrows as the size increases, as has been demonstrated in several recent studies (Fig. S29†).[20,26,59–61]

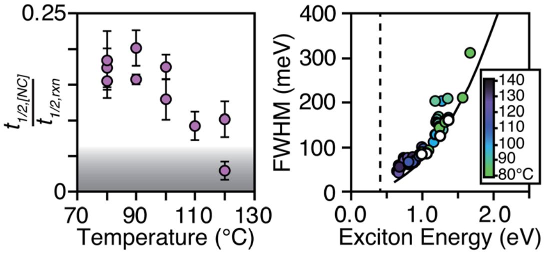

Fig. 7 (A) $t_{1/2,[\mathrm{NC}]}/t_{1/2,\mathrm{rxn}}$ as a function of temperature for a range of *N*,*N*′-4-substituted-phenyl-dodecylthioureas and *N*,*N*′-alkyl-dodecylthioureas. The grey area represents reactions where $t_{1/2,[\mathrm{NC}]} < 2$ s. (B) FWHM and exciton energy plotted for a series of PbS nanocrystals synthesized at 80–140 °C. The intrinsic FWHM of a single size is shown for several PbS sizes (white circles). A fit to the intrinsic FWHM points (black line) is shown to compare with smaller final PbS sizes (FWHM = Ae^{Bx}, $A = 73.8$, $B = 2.33$, x = first excitonic transition energy). The band gap energy of bulk PbS is shown as a dashed black line.

The polydispersity accounts for ~20% of the linewidth at all sizes and is not influenced by the temperature despite the significantly shorter nucleation times at high temperature (Fig. 7B and S28–S30†). Similarly, we find no systematic correlation between precursor and the polydispersity (Fig. S31†), further indication that the precursor reactivity is orthogonal to crystal growth. We conclude that the width of the nucleation phase does not correlate with the polydispersity over a wide range of nucleation times. Hence, the narrow polydispersity must be the result of other mechanisms.

PbSe nanocrystals on the other hand showed systematic changes in polydispersity with temperature (Fig. S28†). The narrowest polydispersities are obtained at 100–120 °C, while lower or higher temperatures both broaden the FWHM. The nonmonotonic change suggests multiple competing factors control the polydispersity in that case. Factors such as the precursor solubility at low temperature or the mixing limited kinetics at high temperature may be important. Regardless, these results do not support the conclusion that the polydispersity is related to the width of the nucleation phase.

Discussion

While it is commonly assumed that colloidal quantum dots are formed from homogeneous solute intermediates (*e.g.* monomers), the identity and concentration of such species is rarely studied. Several pieces of evidence support the formation of solutes in this study. X-Ray PDF patterns acquired *in situ* at early reaction times display molecular length scale correlations rather than extended crystalline order. These signals increase in intensity prior to t_ind and then steadily evolve to a pattern with 1–2 nm pair correlations as the solution develops absorption at 400 nm. Likewise, the transient intermediate observed in the absorption spectra of rapidly quenched aliquots also supports the accumulation of solutes that increase and then decrease in concentration over the course of the reaction (Fig. 6A). However, the species in the *ex situ* and *in situ* measurements are likely distinct given that the PDF measurements are performed prior to the onset of absorption at $\lambda = 400$ nm (albeit at the reaction temperature) while the transient intermediate visible in the spectra of aliquots absorbs strongly at that wavelength. Thus, multiple solute structures are present during nanocrystal growth.

Although the $[\mathrm{PbE}]_\mathrm{ind}$ is an indirect measure of the solute concentration, its sensitivity to the temperature and k_r (Fig. 3) is consistent with the solute generation and consumption mechanism depicted in Scheme 1. Several observations support this conclusion: (1) more rapid precursor conversion kinetics lead to higher $[\mathrm{PbE}]_\mathrm{ind}$, behavior more clearly visible in syntheses of PbSe (Fig. 3B). This is consistent with a growth rate that is orthogonal to the precursor reactivity. (2) Large PbSe nanostructures form more rapidly than PbS under otherwise identical conditions (Fig. 4). More rapid PbSe growth kinetics is consistent with the lower $[\text{PbSe}]_{\text{ind}}$ and the larger final sizes (Fig. 3). (3) The temperature dependence of $[\text{PbE}]_{\text{ind}}$ can be attributed to a changing growth rate; slower growth kinetics at low temperatures leads to higher $[\text{PbE}]_{\text{ind}}$. These pieces of evidence support a homogeneous nucleation and growth mechanism that proceeds *via* the accumulation of solutes generated by precursor conversion.

While a homogeneous nucleation and growth mechanism is consistent with our results, the slow and persistent nucleation kinetics observed here are inconsistent with La Mer's hypothesis that a "burst of nucleation" explains the narrow size distributions typical of these colloids (Fig. 7B). The lack of correlation between the nucleation fractions and the spectral linewidths demonstrates that the length of the nucleation period does not meaningfully influence the polydispersity under these conditions. We therefore conclude that the polydispersity is primarily determined by size distribution focusing mechanisms where small crystals consume solutes more rapidly than large crystals.

Recent studies of InP,[17] CdSe,[62,63] Au,[64] Ag,[65] Ir,[4,66] and Pd,[65] have also documented long nucleation periods and narrow polydispersities. However, the mechanism observed here is distinct from the autocatalytic surface catalyzed conversion mechanism proposed for metal nanocrystals.[4,66] The build-up of persistent solute species and the orthogonality of the precursor conversion and growth kinetics support a distinctly different formation pathway. Nonetheless, it appears that both mechanisms require a size dependent surface reactivity to obtain narrow polydispersities.

Size dependent growth kinetics can also be used to understand the temperature dependence shown in Fig. 5, particularly for PbSe. At the lowest reaction temperatures the ensemble is slow to grow beyond 4 nm in diameter regardless of the solute supply kinetics. A similar observation was recently reported in a study of InP.[17] This behavior suggests self-limiting growth where mature nanocrystals reject solutes that go on to nucleate new crystals. At low temperature relatively small sizes reject solutes and nucleation continues over long periods. At higher temperatures, a broader range of sizes consume solutes, shortening the nucleation process and causing an increased sensitivity of the [NC] to the conversion reactivity. Thus, the influence of temperature on the size can also be understood using a model where growth kinetics are size dependent.

Size dependent growth kinetics are a natural consequence of diffusion limited growth kinetics.[63,66,67] However, the self-limited growth and continuous nucleation at low temperature strongly suggests that diffusion limitations are unlikely to explain the size dependence observed here. A similar conclusion is reached in a related study on PbS to be published elsewhere.[44] More detailed understanding of the factors controlling the growth rate would, therefore, enable the rational optimization of size distributions.

Nucleation mass balance models relate the solute supply kinetics and the number of nanocrystals. Mathematical solutions to those models developed by Sugimoto make the simplifying assumption that nucleation occurs in a narrow range of time and solute concentration. As a result, the rate of crystal growth can be treated as a constant during the nucleation period, and a relatively simple proportionality between the solute supply and consumption and the number of stable nuclei results. While such models are qualitatively consistent with our results (Fig. 5A and B), several other observations made in this study are inconsistent with Sugimoto's underpinning assumptions. The variability of the $[\text{PbE}]_{\text{ind}}$ with the precursor reactivity, the slow and steady increase in the [NC] over a large proportion of the synthesis, and the size dependent growth kinetics all deviate from Sugimoto's picture. Moving beyond this model requires a more detailed understanding of the solute concentration dependence of the nucleation rate as well as the size dependence of the growth rate.

The size dependent growth kinetics and long nucleation periods are also antithetical to classical thermodynamic pictures where nucleation is characterized by a critical radius and critical solute concentration. These pictures only consider the thermodynamic driving force for solute attachment. However, the size dependent growth kinetics are perhaps easier to understand using a mechanism that is defined by a kinetic picture with a barrier to solute attachment. The connection between such mechanisms and the size and polydispersity requires a substantial revision of current thinking about colloidal crystal formation.

Conclusions

We have investigated the influence of reaction temperature on the growth kinetics of PbS and PbSe across more than an order of magnitude in the rate of solute supply. Consistent differences between the induction delay times, final particle size, nucleation duration, and the extent of nucleation could be observed from the reproducible reaction conditions. PbSe nanocrystals nucleate at lower monomer concentrations and with shorter induction delay times than PbS. Together with the relative sizes obtained under otherwise identical conditions, we demonstrate a higher reactivity of PbSe toward growth as compared to PbS. The long nucleation times observed here do not correlate with the polydispersity, indicating that the narrow polydispersities obtained here result from size dependent growth kinetics. The long nucleation times also suggest that classical thermodynamic pictures do not adequately explain colloidal PbS or PbSe nucleation and growth. Moreover, the factors controlling the nanocrystal size distribution result from nanocrystal surface chemistry and its influence on the solute attachment kinetics, rather than the nucleation.

Data availability

Extensive experimental data can be found in the ESI† and is referred to throughout the manuscript!

Author contributions

J. S. O. organized the research. B. M. M., J. D. R., M. W. G., and J. S. O. wrote the manuscript. M. P. C., J. D. R., M. P. H., B. M. M.

collected and analyzed PbS and PbSe dip probe data. B. A., M. W. G., J. D. R., S. K. G. and J. S. O. conceived and designed the *in situ* PbS and PbSe PDF experiments. M. W. G., E. B., N. S., S. K. G., B. A., and J. D. R. helped with collection of the *in situ* PbS and PbSe PDF data. M. W. G. fit PDF patterns and calculated DFT structures of the PbS solute molecules. B. M. M. and M. W. G collected and analyzed UV-Vis-NIR measurement of aliquots taken throughout various PbS reactions and measured the duration of nucleation. M. Y. S. measured the linewidths of PbS and PbSe samples using transient absorption spectroscopy.

Conflicts of interest

The authors declare no competing financial interest.

Acknowledgements

This work was supported by the National Science Foundation under NSF-CHE-2004008. M. W. G. acknowledges support from Brookhaven National Laboratory, National Synchrotron Light Source II Director's Student & Postdoc support program. X-ray scattering data was collected using beamline 28-ID-2 of the National Synchrotron Light Source II, a U.S. DOE Office of Science User Facility operated for the DOE Office of Science by Brookhaven National Laboratory under Contract No. DE-SC0012704. J. D. R acknowledges the Belgian American Education Foundation (B. A. E. F.), Fulbright, Ghent University, and the COMPASS project (H2020-MSCA-RISE-2015-691185) for financial support. B. A. thanks Vincent Klein and the "ELINSTRU" team of the Laboratoire de Physique des Solides for the conception and building of the remotely controlled injector. This research used resources of the Center for Functional Nanomaterials (CFN), which is a U.S. Department of Energy Office of Science User Facility, at Brookhaven National Laboratory under Contract No. DE-SC0012704. The authors acknowledge James P. Shanahan for helpful discussion.

Notes and references

1 J. Park, J. Joo, S. G. Kwon, Y. Jang and T. Hyeon, Synthesis of monodisperse spherical nanocrystals, *Angew. Chem., Int. Ed.*, 2007, **46**(25), 4630–4660.

2 L. S. Hamachi, I. Jen-La Plante, A. C. Coryell, J. De Roo and J. S. Owen, Kinetic Control over CdS Nanocrystal Nucleation Using a Library of Thiocarbonates, Thiocarbamates, and Thioureas, *Chem. Mater.*, 2017, **29**(20), 8711–8719.

3 J. Byun, K. H. Kim, B. K. Kim, J. W. Chang, S. K. Cho and J. J. Kim, Gravimetric analysis of the autocatalytic growth of copper microparticles in aqueous solution, *RSC Adv.*, 2019, **9**(65), 37895–37900.

4 M. A. Watzky and R. G. Finke, Transition metal nanocluster formation kinetic and mechanistic studies. A new mechanism when hydrogen is the reductant: Slow, continuous nucleation and fast autocatalytic surface growth, *J. Am. Chem. Soc.*, 1997, **119**(43), 10382–10400.

5 J. A. Widegren, J. D. Aiken, S. Ozkar and R. G. Finke, Additional investigations of a new kinetic method to follow transition-metal nanocluster formation, including the discovery of heterolytic hydrogen activation in nanocluster nucleation reactions, *Chem. Mater.*, 2001, **13**(2), 312–324.

6 R. Garcia-Rodriguez, M. P. Hendricks, B. M. Cossairt, H. T. Liu and J. S. Owen, Conversion Reactions of Cadmium Chalcogenide Nanocrystal Precursors, *Chem. Mater.*, 2013, **25**(8), 1233–1249.

7 F. Wang, V. N. Richards, S. P. Shields and W. E. Buhro, Kinetics and Mechanisms of Aggregative Nanocrystal Growth, *Chem. Mater.*, 2014, **26**, 5–21.

8 S. Abe, R. K. Capek, B. De Geyter and Z. Hens, Tuning the postfocused size of colloidal nanocrystals by the reaction rate: from theory to application, *ACS Nano*, 2012, **6**(1), 42–53.

9 T. Sugimoto, Preparation of Monodispersed Colloidal Particles, *Adv. Colloid Interface*, 1987, **28**(1), 65–108.

10 C. B. Murray, C. R. Kagan and M. G. Bawendi, Synthesis and characterization of monodisperse nanocrystals and close-packed nanocrystal assemblies, *Annu. Rev. Mater. Sci.*, 2000, **30**, 545–610.

11 Y. Yin and A. P. Alivisatos, Colloidal nanocrystal synthesis and the organic–inorganic interface, *Nature*, 2005, **437**(7059), 664–670.

12 J. S. Owen, E. M. Chan, H. T. Liu and A. P. Alivisatos, Precursor Conversion Kinetics and the Nucleation of Cadmium Selenide Nanocrystals, *J. Am. Chem. Soc.*, 2010, **132**(51), 18206–18213.

13 B. Abecassis, F. Testard, Q. Y. Kong, B. Francois and O. Spalla, Influence of Monomer Feeding on a Fast Cold Nanoparticles Synthesis: Time-Resolved XANES and SAXS Experiments, *Langmuir*, 2010, **26**(17), 13847–13854.

14 B. Abecassis, F. Testard, O. Spalla and P. Barboux, Probing *in situ* the nucleation and growth of gold nanoparticles by small-angle x-ray scattering, *Nano Lett.*, 2007, **7**(6), 1723–1727.

15 M. A. Watzky and R. G. Finke, Transition Metal Nanocluster Formation Kinetic and Mechanistic Studies. A New Mechanism When Hydrogen Is the Reductant: Slow, Continuous Nucleation and Fast Autocatalytic Surface Growth, *J. Am. Chem. Soc.*, 1997, **119**(43), 10382–10400.

16 H. T. Liu, J. S. Owen and A. P. Alivisatos, Mechanistic study of precursor evolution in colloidal group II–VI semiconductor nanocrystal synthesis, *J. Am. Chem. Soc.*, 2007, **129**(2), 305–312.

17 B. M. McMurtry, K. Qian, J. K. Teglasi, A. K. Swarnakar, J. De Roo and J. S. Owen, Continuous Nucleation and Size Dependent Growth Kinetics of Indium Phosphide Nanocrystals, *Chem. Mater.*, 2020, **32**(10), 4358–4368.

18 D. C. Gary, B. A. Glassy and B. M. Cossairt, Investigation of indium phosphide quantum dot nucleation and growth utilizing triarylsilylphosphine precursors, *Chem. Mater.*, 2014, **26**(4), 1734–1744.

19 D. C. Gary, M. W. Terban, S. J. L. Billinge and B. M. Cossairt, Two-Step Nucleation and Growth of InP Quantum Dots *via* Magic-Sized Cluster Intermediates, *Chem. Mater.*, 2015, **27**(4), 1432–1441.

20 J. Cui, A. P. Beyler, I. Coropceanu, L. Cleary, T. R. Avila, Y. Chen, J. M. Cordero, S. L. Heathcote, D. K. Harris, O. Chen, J. S. Cao and M. G. Bawendi, Evolution of the Single-Nanocrystal Photoluminescence Linewidth with Size and Shell: Implications for Exciton-Phonon Coupling and the Optimization of Spectral Linewidths, *Nano Lett.*, 2016, **16**(1), 289–296.

21 D. Franke, D. K. Harris, L. Xie, K. F. Jensen and M. G. Bawendi, The Unexpected Influence of Precursor Conversion Rate in the Synthesis of III-V Quantum Dots, *Angew. Chem., Int. Ed.*, 2015, **54**(48), 14299–14303.

22 H. Sun, F. Wang and W. E. Buhro, Tellurium Precursor for Nanocrystal Synthesis: Tris(dimethylamino)phosphine Telluride, *ACS Nano*, 2018, **12**(12), 12393–12400.

23 K. De Nolf, R. K. Capek, S. Abe, M. Sluydts, Y. Jang, J. C. Martins, S. Cottenier, E. Lifshitz and Z. Hens, Controlling the size of hot injection made nanocrystals by manipulating the diffusion coefficient of the solute, *J. Am. Chem. Soc.*, 2015, **137**(7), 2495–2505.

24 J. Park, A. Jayaraman, X. D. Wang, J. Zhao and H. S. Han, Nanocrystal Precursor Incorporating Separated Reaction Mechanisms for Nucleation and Growth to Unleash the Potential of Heat-up Synthesis, *ACS Nano*, 2020, **14**(9), 11579–11593.

25 J. Park, A. Jayaraman, A. W. Schrader, G. W. Hwang and H.-S. Han, Controllable modulation of precursor reactivity using chemical additives for systematic synthesis of high-quality quantum dots, *Nat. Commun.*, 2020, **11**(1), 5748.

26 M. P. Campos, M. P. Hendricks, A. N. Beecher, W. Walravens, R. A. Swain, G. T. Cleveland, Z. Hens, M. Y. Sfeir and J. S. Owen, A Library of Selenourea Precursors to PbSe Nanocrystals with Size Distributions near the Homogeneous Limit, *J. Am. Chem. Soc.*, 2017, **139**(6), 2296–2305.

27 A. Preske, S. W. O'Neill, B. D. Swartz, J. Liu, O. V. Prezhdo and T. D. Krauss, Size-Programmed Synthesis of PbSe Quantum Dots *via* Secondary Phosphine Chalcogenides, *Chem. Mater.*, 2019, **31**(20), 8301–8307.

28 W.-k. Koh, A. C. Bartnik, F. W. Wise and C. B. Murray, Synthesis of monodisperse PbSe nanorods: a case for oriented attachment, *J. Am. Chem. Soc.*, 2010, **132**(11), 3909–3913.

29 W.-k. Koh, Y. Yoon and C. B. Murray, Investigating the phosphine chemistry of Se precursors for the synthesis of PbSe nanorods, *Chem. Mater.*, 2011, **23**(7), 1825–1829.

30 M. P. Hendricks, M. P. Campos, G. T. Cleveland, I. Jen-La Plante and J. S. Owen, A tunable library of substituted thiourea precursors to metal sulfide nanocrystals, *Science*, 2015, **348**(6240), 1226–1230.

31 J. M. Rhodes, C. A. Jones, L. B. Thal and J. E. Macdonald, Phase-Controlled Colloidal Syntheses of Iron Sulfide Nanocrystals *via* Sulfur Precursor Reactivity and Direct Pyrite Precipitation, *Chem. Mater.*, 2017, **29**(19), 8521–8530.

32 B. A. Tappan, G. Barim, J. C. Kwok and R. L. Brutchey, Utilizing Diselenide Precursors toward Rationally Controlled Synthesis of Metastable $CuInSe_2$ Nanocrystals, *Chem. Mater.*, 2018, **30**(16), 5704–5713.

33 A. C. Berends, W. Van Der Stam, J. P. Hofmann, E. Bladt, J. D. Meeldijk, S. Bals and C. de Mello Donega, Interplay between surface chemistry, precursor reactivity, and temperature determines outcome of ZnS shelling reactions on CuInS2 nanocrystals, *Chem. Mater.*, 2018, **30**(7), 2400–2413.

34 E. Bennett, M. W. Greenberg, A. J. Jordan, L. S. Hamachi, S. Banerjee, S. J. L. Billinge and J. S. Owen, Size Dependent Optical Properties and Structure of ZnS Nanocrystals Prepared from a Library of Thioureas, *Chem. Mater.*, 2022, **34**(2), 706–717.

35 M. P. Camposhttps://www.youtube.com/watch?v=N7Ppv8bj4zc.

36 M. P. Campos, M. P. Hendricks, A. N. Beecher, W. Wslravens, R. A. Swain, G. T. Cleyeland, Z. Hens, M. Y. Sfeir and J. S. Owen, A Library of Selenourea Precursors to PbSe Nanocrystals with Size Distributions near the Homogeneous Limit, *J. Am. Chem. Soc.*, 2017, **139**(6), 2296–2305.

37 T. Sugimoto, F. Shiba, T. Sekiguchi and H. Itoh, Spontaneous nucleation of monodisperse silver halide particles from homogeneous gelatin solution I: silver chloride, *Colloids Surf., A*, 2000, **164**(2–3), 183–203.

38 D. B. K. Chu, J. S. Owen and B. Peters, Nucleation and Growth Kinetics from LaMer Burst Data, *J. Phys. Chem. A*, 2017, **121**(40), 7511–7517.

39 A. W. Jansons, L. K. Plummer and J. E. Hutchison, Living Nanocrystals, *Chem. Mater.*, 2017, **29**(13), 5415–5425.

40 I. Moreels, K. Lambert, D. De Muynck, F. Vanhaecke, D. Poelman, J. C. Martins, G. Allan and Z. Hens, Composition and size-dependent extinction coefficient of colloidal PbSe quantum dots, *Chem. Mater.*, 2007, **19**(25), 6101–6106.

41 R. S. Kane, R. E. Cohen and R. Silbey, Theoretical study of the electronic structure of PbS nanoclusters, *J. Phys. Chem.*, 1996, **100**(19), 7928–7932.

42 H. X. Zeng, Z. A. Schelly, K. Ueno-Noto and D. S. Marynick, Density functional study of the structures of lead sulfide clusters (PbS)(*n*) (*n*=1–9), *J. Phys. Chem. A*, 2005, **109**(8), 1616–1620.

43 S. Wu, H. Zeng and Z. A. Schelly, Preparation of Ultrasmall, Uncapped PbS Quantum Dots *via* Electroporation of Vesicles, *Langmuir*, 2005, **21**(2), 686–691.

44 B. Abécassis; M. W. Greenberg; V. Bal; B. M. McMurtry; M. P. Campos; L. Guillemeney; B. Mahler; S. Prevost; L. Sharpnack; M. P. Hendricks; D. DeRosha; E. Bennett; N. Saenz; B. Peters and J. S. Owen, *Persistent Nucleation and Size Dependent Attachment Kinetics Produce Monodisperse PbS Nanocrystals*. In Revision.

45 V. S. Gurin, K. N. Kasparov and E. A. Tyavlovskaya, Formation and XPS characterization of small lead sulfide clusters, *Colloids Surf., A*, 1998, **139**(1), 1–5.

46 J. Workman Jr. and L. Weyer, *Practical Guide to Interpretive Near-Infrared Spectroscopy*. 1st edn; CRC Press, 2007.

47 L. Cademartiri, E. Montanari, G. Calestani, A. Migliori, A. Guagliardi and G. A. Ozin, Size-dependent extinction

coefficients of PbS quantum dots, *J. Am. Chem. Soc.*, 2006, **128**(31), 10337–10346.

48 I. Moreels, K. Lambert, D. Smeets, D. De Muynck, T. Nollet, J. C. Martins, F. Vanhaecke, A. Vantomme, C. Delerue, G. Allan and Z. Hens, Size-Dependent Optical Properties of Colloidal PbS Quantum Dots, *ACS Nano*, 2009, **3**(10), 3023–3030.

49 We note that solutes may continue depositing on nanocrystals after the aliquot is removed from solution and thus the yield of PbS and the radius may not reflect the conditions at the moment the aliquot was extracted. Despite these complications, the kinetics extracted using the *in situ* absorption and aliquoting methods are similar.

50 A. P. Hammersley, *Fit2d v12. 012 reference manual v6.0*, Internal Report, 2004, ESRF98HA01T.

51 P. Juhas, T. Davis, C. L. Farrow and S. J. L. Billinge, PDFgetX3: a rapid and highly automatable program for processing powder diffraction data into total scattering pair distribution functions, *J. Appl. Crystallogr.*, 2013, **46**, 560–566.

52 X. Yang; P. Juhas; C. L. Farrow and S. J. Billinge, xPDFsuite: an end-to-end software solution for high throughput pair distribution function transformation, visualization and analysis. arXiv preprint arXiv:1402.3163, 2014.

53 C. L. Farrow, P. Juhas, J. W. Liu, D. Bryndin, E. S. Bozin, J. Bloch, T. Proffen and S. J. L. Billinge, PDFfit2 and PDFgui: computer programs for studying nanostructure in crystals, *J. Phys.: Condens. Matter*, 2007, **19**(33), 335129.

54 E. D. Bojesen and B. B. Iversen, The chemistry of nucleation, *Crystengcomm*, 2016, **18**(43), 8332–8353.

55 K. M. O. Jensen, M. Christensen, P. Juhas, C. Tyrsted, E. D. Bojesen, N. Lock, S. J. L. Billinge and B. B. Iversen, Revealing the Mechanisms behind SnO_2 Nanoparticle Formation and Growth during Hydrothermal Synthesis: An *In Situ* Total Scattering Study, *J. Am. Chem. Soc.*, 2012, **134**(15), 6785–6792.

56 D. Saha, K. M. O. Jensen, C. Tyrsted, E. D. Bojesen, A. H. Mamakhel, A. C. Dippel, M. Christensen and B. B. Iversen, *In Situ* Total X-Ray Scattering Study of WO3 Nanoparticle Formation under Hydrothermal Conditions, *Angew. Chem., Int. Ed.*, 2014, **53**(14), 3667–3670.

57 M. W. Terban, D. Banerjee, S. Ghose, B. Medasani, A. Shukla, B. A. Legg, Y. Zhou, Z. Zhu, M. L. Sushko, J. J. De Yoreo, J. Liu, P. K. Thallapally and S. J. L. Billinge, Early stage structural development of prototypical zeolitic imidazolate framework (ZIF) in solution, *Nanoscale*, 2018, **10**(9), 4291–4300.

58 K. Kodama, S. Iikubo, T. Taguchi and S. Shamoto, Finite size effects of nanoparticles on the atomic pair distribution functions, *Acta Crystallogr. A*, 2006, **62**, 444–453.

59 P. B. Green, P. Narayanan, Z. Q. Li, P. Sohn, C. J. Imperiale and M. W. B. Wilson, Controlling Cluster Intermediates Enables the Synthesis of Small PbS Nanocrystals with Narrow Ensemble Line Widths, *Chem. Mater.*, 2020, **32**(9), 4083–4094.

60 O. Voznyy, L. Levina, J. Z. Fan, M. Askerka, A. Jain, M. J. Choi, O. Ouellette, P. Todorovic, L. K. Sagar and E. H. Sargent, Machine Learning Accelerates Discovery of Optimal Colloidal Quantum Dot Synthesis, *Acs Nano*, 2019, **13**(10), 11122–11128.

61 J. Ryu, S. D. Park, D. Baranov, I. Rreza, J. S. Owen and D. M. Jonas, Relations between absorption, emission, and excited state chemical potentials from nanocrystal 2D spectra, *Sci. Adv.*, 2021, **7**(22), eabf4741.

62 B. Abecassis, C. Bouet, C. Garnero, D. Constantin, N. Lequeux, S. Ithurria, B. Dubertret, B. R. Pauw and D. Pontoni, Real-Time *in Situ* Probing of High-Temperature Quantum Dots Solution Synthesis, *Nano Lett.*, 2015, **15**(4), 2620–2626.

63 P. T. Prins, F. Montanarella, K. Dumbgen, Y. Justo, J. C. van der Bok, S. O. M. Hinterding, J. J. Geuchies, J. Maes, K. De Nolf, S. Deelen, H. Meijer, T. Zinn, A. V. Petukhov, F. T. Rabouw, C. De Mello Donega, D. Vanmaekelbergh and Z. Hens, Extended Nucleation and Superfocusing in Colloidal Semiconductor Nanocrystal Synthesis, *Nano Lett.*, 2021, **21**(6), 2487–2496.

64 J. Turkevich, P. C. Stevenson and J. Hillier, A Study of the Nucleation and Growth Processes in the Synthesis of Colloidal Gold, *Discuss. Faraday Soc.*, 1951, **11**, 55–75.

65 S. Mozaffari, W. H. Li, C. Thompson, S. Ivanov, S. Seifert, B. Lee, L. Kovarik and A. M. Karim, Colloidal nanoparticle size control: experimental and kinetic modeling investigation of the ligand metal binding role in controlling the nucleation and growth kinetics, *Nanoscale*, 2017, **9**(36), 13772–13785.

66 D. R. Handwerk, P. D. Shipman, C. B. Whitehead, S. Ozkar and R. G. Finke, Mechanism-Enabled Population Balance Modeling of Particle Formation en Route to Particle Average Size and Size Distribution Understanding and Control, *J. Am. Chem. Soc.*, 2019, **141**(40), 15827–15839.

67 X. G. Peng, J. Wickham and A. P. Alivisatos, Kinetics of II–VI and III–V colloidal semiconductor nanocrystal growth: "Focusing" of size distributions, *J. Am. Chem. Soc.*, 1998, **120**(21), 5343–5344.